Dynamics of confined suspensions of swimming particles

2009 J. Phys.: Condens. Matter 21 204107

(http://iopscience.iop.org/0953-8984/21/20/204107)

IOP Publishing Journal of Physics: Condensed Matter

J. Phys.: Condens. Matter **21** (2009) 204107 (13pp) doi:10.1088/0953-8984/21/20/204107

Dynamics of confined suspensions of swimming particles

Juan P Hernandez-Ortiz[1], Patrick T Underhill[2] and Michael D Graham[2]

[1] Departamento de Materiales, Universidad Nacional de Colombia Sede Medellín, Carrera 80 # 65-223, Bloque M3-050, Medellín, Colombia
[2] Department of Chemical and Biological Engineering, University of Wisconsin-Madison, Madison, WI 53706-1691, USA

E-mail: graham@engr.wisc.edu

Received 1 August 2008, in final form 17 October 2008
Published 21 April 2009
Online at stacks.iop.org/JPhysCM/21/204107

Abstract

Low Reynolds number direct simulations of large populations of hydrodynamically interacting swimming particles confined between planar walls are performed. The results of simulations are compared with a theory that describes dilute suspensions of swimmers. The theory yields scalings with concentration for diffusivities and velocity fluctuations as well as a prediction of the fluid velocity spatial autocorrelation function. Even for uncorrelated swimmers, the theory predicts anticorrelations between nearby fluid elements that correspond to vortex-like swirling motions in the fluid with length scale set by the size of a swimmer and the slit height. Very similar results arise from the full simulations indicating either that correlated motion of the swimmers is not significant at the concentrations considered or that the fluid phase autocorrelation is not a sensitive measure of the correlated motion. This result is in stark contrast with results from unconfined systems, for which the fluid autocorrelation captures large-scale collective fluid structures. The additional length scale (screening length) introduced by the confinement seems to prevent these large-scale structures from forming.

(Some figures in this article are in colour only in the electronic version)

1. Introduction

Experimental observations of suspensions of swimming micro-organisms illustrate a number of fascinating phenomena that are still poorly understood. Correlations of the swimmers result in jets and swirling motions on scales larger than that of a single organism [1, 2]. The organisms also form local nematic ordering though they have no global nematic behavior [3]. The collective behavior leads to swimmer velocities larger than that of an isolated organism [4] and enhanced transport in the fluid [5].

There are many open questions regarding these important observations both in terms of what leads to the phenomena and their biological significance. Some models consider 'local' interactions between nearby organisms within a finite range, and how those can lead to large-scale collective behavior. These interactions may take the form of ad hoc rules [6] or direct steric interactions between the swimmers [7]. Other models consider long-ranged hydrodynamic interactions between swimmers, which decay as r^{-2} in an unbounded domain [8–12]. The relative importance of these phenomena is still not fully understood.

Many experiments observing these phenomena have been performed in droplets or thin films, but the influence of confinement on the observations is not clear. Confinement sterically hinders the organisms and also affects the hydrodynamic interactions, both between the organisms and between the organism and the boundary. The boundaries may also play a role in transport of nutrients, which may, in turn, affect motion of the organisms. For example, oxygen levels may be different near surfaces, altering the motion of the organisms. For droplets or films, the rigidity of the surface from secreted molecules may affect the fluid boundary condition and dynamics of the organisms [4, 3].

Most experiments mentioned above have concentrated on two types of bacteria, *E. coli* and *B. subtilis*. Both organisms use flagella to propel themselves forward through

the fluid. However, other types of organisms propel through a fluid by other mechanisms, such as pulling themselves forward from the front [13]. What role the propulsion method plays on the collective behavior has not been clarified, although computational and theoretical evidence suggests that organisms pushed from behind display more complex collective behavior than those pulled from the front [14, 12]. In general, what biological significance the above phenomena play in the function of the micro-organisms remains unclear.

In this article we focus on the role that confinement plays in the collective behavior. The only prior publication using computational models to investigate how hydrodynamic interactions affect the collective behavior of swimming micro-organisms in confined environments is by Hernández *et al* [8]. They showed that hydrodynamic interactions were sufficient to produce many qualitative phenomena seen in experiments, including increased transport and swirls in the fluid. We focus on confined systems not only because many experiments have been done in confined environments, but also to draw comparisons with unconfined dynamics. Simulations in three-dimensional periodic domains have shown changes in dynamics with the size of the domain [12] that are thought to arise because of long-range structures that fill the entire domain. Some experiments have attempted to measure unconfined dynamics by examining the response far away from the confining walls [15–17]. However, because of the long-ranged nature of hydrodynamics, the point at which confined systems with very large gaps reduces to an unconfined system is not obvious.

We examine the behavior at different levels of confinement and at different concentrations ranging from the dilute limit into the semidilute regime. However the concentration is still low enough that we do not expect the steric interactions between the organisms to be the dominant interaction and lead to nematic-like structures. Instead we expect the long-ranged hydrodynamic interactions to play an important role. The confinement boundaries alter these hydrodynamic interactions. The walls also induce a non-uniform concentration profile within the domain, with the organisms concentrating at the walls. Finally, the walls introduce a new length scale which screens hydrodynamics and alters flow structures over larger length scales. We will show in this article how the dynamics depend on confinement and how they compare with theoretical predictions.

2. Swimmer model

Consider a suspension of N neutrally buoyant rod-like swimmers confined between two planar walls. Directions x_1 and x_2 are periodic of side length L, and the walls are separated in the x_3-direction by a distance $2H$. Each swimmer has a characteristic length ℓ, a characteristic width w, and in isolation would move in a straight line with a speed v_{is}. It is assumed that the Reynolds number, $Re = v_{\text{is}}H/\nu \ll 1$, where ν is the fluid kinematic viscosity, in which case the fluid motion is governed by the Stokes equation. To allow treatment of large populations ($>10^3$ swimmers) over long times, a very simple model of each swimmer is adopted, following our previous work [8, 12].

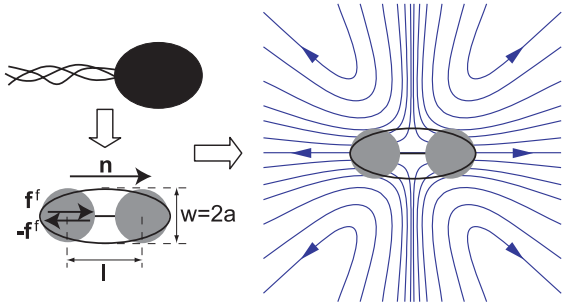

Figure 1. Illustration of a pushing organism, our swimmer model, and the fluid disturbance they cause in an unbounded domain. Our model shows the hydrodynamic radius of the beads and the ellipsoidal excluded volume. The double-arrow signifies the phantom flagellum force acting on the bead and an opposite force acting on the fluid. Both forces act at the center of the first bead. The blue lines represent streamlines of the axisymmetric fluid disturbance. A puller would produce the same streamlines, but with the direction of the velocities reversed.

Each self-propelled particle is modeled as two beads connected by a stiff spring with equilibrium length ℓ as shown in figure 1. The unit vector pointing along the swimmer axis from bead 1 to bead 2 is denoted $\mathbf{n}$. Propulsion is provided by a 'phantom flagellum' that we do not treat explicitly, but only through its effect on the swimmer body and the fluid. The bead which is connected to the flagellum, denoted bead 1, feels a force $\mathbf{f}^{\text{f}}$ exerted on it. However, the flagellum also exerts a force $-\mathbf{f}^{\text{f}}$ on the fluid. This force on the fluid occurs at the position of bead 1. With this model we can consider 'pushers' or 'pullers' depending on whether $\mathbf{f}^{\text{f}}$ is parallel or anti-parallel to $\mathbf{n}$, respectively. A pusher sends fluid away from it fore and aft, with fluid moving toward its 'waist', and vice versa for a puller. Whether a real swimmer is a pusher or a puller depends on the specific mechanism of locomotion (cf [13])—a cell whose flagella propel it forward predominantly from behind would be a pusher [8, 12]. We will focus primarily on pushers in this article, though some results with pullers are presented.

To measure the concentration of the swimmers we define an effective volume fraction $\phi_{\text{e}} = \pi N\ell^3/(12L^2H)$—this would be the true volume fraction if the swimmers were spheres of diameter ℓ. In the present geometry, swimmers in dilute systems form layers near the two walls. Therefore, we find it convenient to also define an effective area fraction if all swimmers resided in the layers. It is defined as $\psi_{\text{e}} = C\pi N\ell^2/(4L^2)$, where the constant $C = 1/2$ if the gap is large enough to allow for a layer at each wall ($2H > 2w$), or $C = 1$ for extreme confinements, e.g. monolayers.

The force in the 'stiff' connector between the beads follows a finitely extensible nonlinear elastic (FENE) spring model with a non-zero equilibrium length equal to the swimmer size ℓ [18]:

$$\mathbf{f}^{\text{c}}_{\nu,k} = h\mathbf{Q}_\nu \frac{1 - \ell/|\mathbf{Q}_\nu|}{1 - [(|\mathbf{Q}_\nu| - \ell)/(\ell_{\text{m}} - \ell)]^2}, \qquad (1)$$

where h is the spring constant, $\mathbf{Q}_\nu$ is the connector vector from bead 1 to bead 2 on swimmer ν, and ℓ_m is the swimmer maximum size. With this spring law, the swimmer will shrink slightly for a pushing flagellum, or expand for a pulling one. The values of h and ℓ_m are chosen so that the spring approximates a rigid constraint while still allowing timesteps that are not prohibitively small. For the results presented here, $h = \mathrm{f}^\mathrm{f}/(0.1\ell)$ and $\ell_\mathrm{m} = 1.15\ell$. The swimmers also interact through an excluded volume potential, which is taken as the repulsive portion of the Gay–Berne potential [19]; this potential is widely used in molecular simulations to model steric repulsions between rod-like objects. The size and aspect ratio of the excluded volume potential to related to the size of the swimmer ℓ and the hydrodynamic radius of a bead a as illustrated in figure 1. The width of the excluded volume is taken as $w = 2a$ and the length as $\ell + 2a$. This means that the excluded volume restricts bead positions such that the hydrodynamic radii do not overlap. It also gives an aspect ratio of $\gamma = 1 + \ell/(2a)$. The model presented here has $\ell = 3a$, and therefore an aspect ratio of $\gamma = 2.5$.

The motion of the swimmers is determined by the force balance (neglecting inertia because of the small size of a microorganism) for each bead ($k = 1, 2$) of a swimmer ν, as follows

$$\mathbf{f}^\mathrm{h}_{\nu,k} + \mathbf{f}^\mathrm{c}_{\nu,k} + \mathbf{f}^\mathrm{x}_{\nu,k} + \delta_{k1}\mathbf{f}^\mathrm{f}_\nu = 0 \qquad \text{for } k = 1, 2, \tag{2}$$

where δ_{ij} is the Kronecker delta, $\mathbf{f}^\mathrm{h}_{\nu,k}$ is the hydrodynamic drag force, $\mathbf{f}^\mathrm{c}_{\nu,k}$ is the connector (spring) force and $\mathbf{f}^\mathrm{x}_{\nu,k}$ are the bead–bead, bead–swimmer and bead–wall excluded volume forces. Notice that the force balance for bead 1 differs from the balance on bead 2 by the presence of the flagellum force, $\mathbf{f}^\mathrm{f}_\nu$.

In our simulations, each bead will be treated as a point particle. In this situation, the hydrodynamic drag force on a bead k of swimmer ν is given by a generalization of Stokes' law [20]:

$$\mathbf{f}^\mathrm{h}_{\nu,k} = -\zeta\left(\mathbf{v}_{\nu,k} - \mathbf{u}_{\nu,k}\right), \tag{3}$$

where $\zeta = 6\pi\eta a$ is the Stokes drag coefficient on a bead with hydrodynamic radius a in a fluid with viscosity η, $\mathbf{v}_{\nu,k} = \dot{\mathbf{x}}_{\nu,k}$ is the velocity of the bead, where $\mathbf{x}_{\nu,k}$ is the position (Cartesian coordinates) of the bead, and $\mathbf{u}_{\nu,k}$ is the fluid velocity at the bead position. There are two contributions to this fluid velocity: the first is the motion driven by the forces exerted by the other beads (and flagella) in the system, and the second is the correction to the velocity experienced by the bead due to the presence of confining walls. This correction leads for example to the decrease in bead mobility found in a confining geometry. Both of these contributions are determined simultaneously by the methodology used here. Equations (3) and (2) give an evolution equation for the bead positions as follows,

$$\frac{\mathrm{d}\mathbf{x}_{\nu,k}}{\mathrm{d}t} = \mathbf{u}_{\nu,k} + \frac{1}{\zeta}\left(\mathbf{f}^\mathrm{c}_{\nu,k} + \mathbf{f}^\mathrm{x}_{\nu,k} + \delta_{1k}\mathbf{f}^\mathrm{f}_\nu\right). \tag{4}$$

For $Re = 0$, the fluid velocity at a point $\mathbf{x}$ due to a collection of point-forces is calculated by summing over all forces times the Green's function $\mathbf{G}$ for the Stokes equation for the geometry and boundary conditions of interest. Considering the beads of each of the N swimmers as point-forces and including the disturbance due to the phantom flagellum, we write the fluid velocity at a point $\mathbf{x}$ as

$$\mathbf{u}(\mathbf{x}) = \sum_{\mu=1}^{N}\sum_{l=1}^{2}\mathbf{G}(\mathbf{x}, \mathbf{x}_{\mu,l})\cdot\left(-\mathbf{f}^\mathrm{h}_{\mu,l} - \delta_{l1}\mathbf{f}^\mathrm{f}_\mu\right), \tag{5}$$

where the first term represents the direct hydrodynamic forces exerted by the beads on the fluid and the second term represents the disturbance caused by the phantom flagella. These two contributions can be combined using the force balance on each bead to become

$$\mathbf{u}(\mathbf{x}) = \sum_{\mu=1}^{N}\sum_{l=1}^{2}\mathbf{G}(\mathbf{x}, \mathbf{x}_{\mu,l})\cdot\left(\mathbf{f}^\mathrm{c}_{\mu,l} + \mathbf{f}^\mathrm{x}_{\mu,l}\right). \tag{6}$$

Similarly, the fluid velocity at the position of a bead k of swimmer ν is calculated by excluding the singular part of the fluid velocity generated by the bead:

$$\mathbf{u}_{\nu,k} = \sum_{\mu=1}^{N}\sum_{l=1}^{2}(\mathbf{G}(\mathbf{x}_{\nu,k}, \mathbf{x}_{\mu,l}) - \delta_{\nu\mu}\delta_{kl}\mathbf{G}_\infty(\mathbf{x}_{\nu,k} - \mathbf{x}_{\mu,l}))\cdot\left(\mathbf{f}^\mathrm{c}_{\mu,l} + \mathbf{f}^\mathrm{x}_{\mu,l}\right). \tag{7}$$

Here $\mathbf{G}_\infty$ is the Oseen–Burgers or Stokeslet tensor, the free-space point-force Green's function for Stokes equation. It is given explicitly as

$$\mathbf{G}_\infty(\mathbf{x}) = \frac{1}{8\pi\eta r}\left(\boldsymbol{\delta} + \frac{\mathbf{x}\mathbf{x}}{r^2}\right) \tag{8}$$

with $r = |\mathbf{x}|$ and $\boldsymbol{\delta}$ the identity tensor. In an unbounded domain, $\mathbf{G}$ and $\mathbf{G}_\infty$ are identical so the $\nu = \mu$, $k = l$ terms in this expression are zero. In a bounded domain, however, $\mathbf{G}$ contains a finite correction due to the change in the flow induced by the boundaries; subtracting off $\mathbf{G}_\infty$ when $\nu = \mu$, $k = l$ reveals this finite correction in the overall expression. Substitution of equation (7) into the evolution equation for the bead positions, equation (4), results in

$$\frac{\mathrm{d}\mathbf{x}_{\nu,k}}{\mathrm{d}t} = \frac{1}{\zeta}\left(\delta_{1k}\mathbf{f}^\mathrm{f}_\nu\right) + \sum_{\mu=1}^{N}\sum_{l=1}^{2}\mathbf{M}_{(\nu,k)(\mu,l)}\cdot\left(\mathbf{f}^\mathrm{c}_{\mu,l} + \mathbf{f}^\mathrm{x}_{\mu,l}\right). \tag{9}$$

Here $\mathbf{M}_{(\nu,k)(\mu,l)}$ is a 3×3 tensor which constitutes a block of the $(3\times 2N)\times(3\times 2N)$ mobility tensor, $\mathbf{M}$: [21]

$$\mathbf{M}_{(\nu,l)(\mu,k)} = \delta_{\nu\mu}\delta_{kl}\frac{\boldsymbol{\delta}}{\zeta} + (\mathbf{G}(\mathbf{x}_{\nu,k}, \mathbf{x}_{\mu,l}) - \delta_{\nu\mu}\delta_{kl}\mathbf{G}_\infty(\mathbf{x}_{\nu,k} - \mathbf{x}_{\mu,l})). \tag{10}$$

Equation (9) can be written in a compact form by introducing $3\times 2N$ dimensional vectors containing the coordinates and forces of all beads as follows:

$$\frac{\mathrm{d}}{\mathrm{d}t}\mathbf{R} = \frac{1}{\zeta}\mathbf{F}^\mathrm{f} + \mathbf{M}\cdot\mathbf{F}^\mathrm{b}, \tag{11}$$

where $\mathbf{R}$ contains the coordinates of all beads, $\mathbf{F}^\mathrm{f}$ is a vector with the flagellum force, whose components are non-zero for bead 1 of each swimmer, and $\mathbf{F}^\mathrm{b}$ is a vector containing the total non-hydrodynamic and non-flagellar forces on each bead.

The net force exerted by an isolated swimmer on the fluid is zero—to leading order in the far field a neutrally buoyant

swimmer is a force dipole. The present approach captures this universal far-field behavior while neglecting the near-field corrections to the hydrodynamic interactions between swimmers, which are dependent on the details of the organism. The validity of this approximation is supported by recent simulation results [11]. Finally, we note that the limited set of results we have obtained with multi-bead rod swimmers is qualitatively consistent with those for the two-bead swimmers.

The fluid velocity $\mathbf{M}\cdot\mathbf{F}^{\mathrm{b}}$ is calculated using the general geometry Ewald-like method (GGEM) introduced by Hernández-Ortiz *et al* [22]. A brief description of the GGEM starts with considering the Stokes system of equations for a flow driven by a distribution of $2N$ point-forces,

$$-\nabla p(\mathbf{x})+\eta\nabla^2\mathbf{u}(\mathbf{x})=-\boldsymbol{\rho}(\mathbf{x})\qquad \nabla\cdot\mathbf{u}(\mathbf{x})=0, \tag{12}$$

where η is the fluid viscosity and the force density is $\boldsymbol{\rho}(\mathbf{x})=\sum_{\nu=1}^{2N}\mathbf{f}_\nu\delta(\mathbf{x}-\mathbf{x}_\nu)$. Here $\mathbf{f}_\nu$ is the force exerted on the fluid at point $\mathbf{x}_\nu$. The solution of (12), can be written in the form of (6) and combined into the $\mathbf{M}\cdot\mathbf{F}$ product. If computed explicitly, this product is a matrix–vector operation that requires $\mathrm{O}(N^2)$ calculations. GGEM determines the product implicitly for any geometry (with appropriate boundary conditions) without performing the matrix–vector manipulations. It starts with the restatement of the force–density expression in (12), $\boldsymbol{\rho}(\mathbf{x})=\boldsymbol{\rho}_{\mathrm{l}}(\mathbf{x})+\boldsymbol{\rho}_{\mathrm{g}}(\mathbf{x})$ using a smoothing function g, similar to conventional particle-mesh methods. By linearity of the Stokes equation, the fluid velocity is written as a sum of two parts, the solution with each force–density separately. The 'local density'

$$\boldsymbol{\rho}_{\mathrm{l}}(\mathbf{x})=\sum_{\nu=1}^{2N}\mathbf{f}_\nu[\delta(\mathbf{x}-\mathbf{x}_\nu)-g(\mathbf{x}-\mathbf{x}_\nu)] \tag{13}$$

drives a local velocity, $\mathbf{u}_{\mathrm{l}}(\mathbf{x})$, which is calculated assuming an unbounded domain: $\mathbf{u}_{\mathrm{l}}(\mathbf{x})=\sum_\nu^N\mathbf{G}_{\mathrm{l}}(\mathbf{x}-\mathbf{x}_\nu)\cdot\mathbf{f}_\nu$, where $\mathbf{G}_{\mathrm{l}}(\mathbf{x})$ is composed of the free-space Green's function $\mathbf{G}_\infty$ minus a smoothed Stokeslet obtained from the solution of Stokes equations with the forcing term modified by the smoothing function g. For the Stokes equations we found that a modified Gaussian smoothing function defined by

$$g(r)=(\alpha^3/\pi^{3/2})\mathrm{e}^{(-\alpha^2r^2)}(5/2-\alpha^2r^2) \tag{14}$$

yields a simple expression for $\mathbf{G}_{\mathrm{l}}(\mathbf{x})$:

$$\mathbf{G}_{\mathrm{l}}(\mathbf{x})=\frac{1}{8\pi\eta}\left(\boldsymbol{\delta}+\frac{\mathbf{xx}}{r^2}\right)\frac{\mathrm{erfc}(\alpha r)}{r}-\frac{1}{8\pi\eta}\left(\boldsymbol{\delta}-\frac{\mathbf{xx}}{r^2}\right)\frac{2\alpha}{\pi^{1/2}}\mathrm{e}^{(-\alpha^2r^2)}. \tag{15}$$

Because $\mathbf{G}_{\mathrm{l}}(\mathbf{x})$ decays exponentially on the length scale α^{-1}, in practice the local velocity can be computed, as in normal Ewald methods, by only considering near-neighbors to each particle ν [23].

For the present work, the point-particle approximation is not desired; in particular, as the concentration of particles increases, the probability that particles will overlap, having unphysical velocities, increases. To avoid this problem, the bead hydrodynamic radius, a, can be used to define a new smoothed-force density which will give a non-singular velocity. This is achieved by replacing the Stokeslet by a regularized Stokeslet, using the same modified Gaussian with α replaced by ξ, with $\xi\sim a^{-1}$, yielding

$$\mathbf{G}_{\mathrm{l}}^{\mathrm{R}}(\mathbf{x})=\frac{1}{8\pi\eta}\left(\boldsymbol{\delta}+\frac{\mathbf{xx}}{r^2}\right)\left[\frac{\mathrm{erf}(\xi r)}{r}-\frac{\mathrm{erf}(\alpha r)}{r}\right]+\frac{1}{8\pi\eta}\left(\boldsymbol{\delta}-\frac{\mathbf{xx}}{r^2}\right)\left(\frac{2\xi}{\pi^{1/2}}\mathrm{e}^{(-\xi^2r^2)}-\frac{2\alpha}{\pi^{1/2}}\mathrm{e}^{(-\alpha^2r^2)}\right), \tag{16}$$

where the superscript R stands for regularized force density. For $\xi^{-1}=3a/\sqrt{\pi}$, the maximum fluid velocity is equal to that of a particle with radius a and the pair mobility remains positive-definite [22, 24].

The global velocity, $\mathbf{u}_{\mathrm{g}}(\mathbf{x})$, is due to the force distribution $\boldsymbol{\rho}_{\mathrm{g}}(\mathbf{x})$, which is given by

$$\boldsymbol{\rho}_{\mathrm{g}}(\mathbf{x})=\sum_{\nu=1}^{2N}\mathbf{f}_\nu g(\mathbf{x}-\mathbf{x}_\nu). \tag{17}$$

For a general domain, we find the solution to Stokes' equation numerically, requiring that $\mathbf{u}_{\mathrm{l}}+\mathbf{u}_{\mathrm{g}}$ satisfy appropriate boundary conditions. At a no-slip boundary we would require $\mathbf{u}_{\mathrm{g}}(\mathbf{x})=-\mathbf{u}_{\mathrm{l}}(\mathbf{x})$. For problems with periodic boundary conditions, Fourier techniques can be used to guarantee the periodicity of the global velocity $\mathbf{u}_{\mathrm{g}}$. The periodicity on the local velocity, $\mathbf{u}_{\mathrm{l}}$, is obtained using the minimum image convention. In the present case, the global contribution is calculated on a mesh with $M=M_1M_2M_3$ mesh points, with M_1, M_2, and M_3 the number of mesh points in the x_1, x_2, and x_3 directions. A fast Fourier transform (FFT) method is used in the two periodic directions (x_1 and x_2) and a second order finite difference method (FDM) scheme for the confined direction (x_3). The FFT is implemented using FFTW [25, 26], while the FDM is solved with a regular LU decomposition routine [27].

For GGEM, the results should be independent of α but the computational cost of the local and global calculations depend on α. Therefore, we choose the optimal α which minimizes the total computational cost. In the global calculation, to have an accurate solution, the mesh size must be smaller than the scale of the smoothing function, which is α^{-1}. Therefore, $M_{1,2,3}\sim\alpha$. The cost of the each LU decomposition scales as M_3^3 and there are M_1M_2 number of them, giving a total global cost that scales as α^5. Note that the cost of each FFT scales as $M_1M_2\ln(M_1M_2)$ and there are M_3 of them giving a scaling of $\alpha^3\ln(\alpha)$. This is small compared to the cost of the LU decomposition. In the local calculation, the contribution of all pairs must be calculated that lie within a neighbor list determined by the decay of the local Green's function. The local Green's function decays over a distance α^{-1}, so the number of neighbors for each particle scales as $N\alpha^{-3}$. The calculation must be performed over all pairs, which is the number of particles times the number of neighbors per particle, resulting in a local calculation cost scaling of $N^2\alpha^{-3}$. Minimizing the total (local and global) computational cost with respect to α gives an optimal α that scales as $\alpha_{\mathrm{opt}}\sim N^{1/4}$ and a total cost that scales as $\mathrm{O}(N^{5/4})$. If we had chosen a different, linear, method for the FDM calculation, the global cost would have scaled as α^3, leading to an optimal value of $\alpha_{\mathrm{opt}}\sim N^{1/3}$ and a total computational cost that scaled as $\mathrm{O}(N)$.

For our slit geometry, we used for the periodic directions a number of mesh points $M_{1,2} = \sqrt{2}\alpha L$ while $M_3 = 4\sqrt{2}\alpha H$ for the confined direction. The previous analysis determined how the optimal value of α changes with system size N. However, to determine the value of the prefactor, and thus the value of α used in the simulations, the cost of the global and local contributions must be determined on the computers used for the computation. For our machines, determining the computational cost led to using $\alpha_{\rm opt} = 0.042N^{1/4}$.

3. Theory for dilute suspensions

As a starting point for understanding the dynamics of confined suspensions of swimmers, we present here a scaling theory valid in the dilute limit, in which the swimmers act almost independently. We also show the fluid correlations for a suspension of uncorrelated swimmers. These properties are an important baseline in order to identify whether or not an observed feature of a swimming suspension arises from collective dynamics.

3.1. Diffusivity and velocity scaling

In the dilute limit, swimmers are mostly to be found in layers near each wall [8]. The fundamental reason for this is simple—a swimmer that is not near a wall is in all likelihood oriented toward one wall or the other and will eventually collide with it. Once it collides with a wall it remains there until a fluctuation causes it to leave (in which case it will eventually hit the other wall). We shall see that swimmer–wall hydrodynamic interactions have a quantitative effect on the layering, but not a qualitative one. Recent experiments with bacteria also show a very high concentration at the walls [28]. Because the formation of layers is a generic phenomenon, the present theory focuses on the dynamics of swimmers in the layers.

In the absence of other swimmers, a swimmer will continue in a straight line within the layer. Collisions or hydrodynamic interactions with other swimmers cause the direction of swimming to change, leading to diffusive motion at long timescales. From a scaling perspective, consider a random walk in which the particle swims at constant speed $v_{\rm s}$ along a trajectory for a mean duration $\tau_{\rm s}$ before changing directions. The motion at long times is diffusive with a diffusivity that scales as $D_{\rm s} \sim v_{\rm s}^2\tau_{\rm s} \sim v_{\rm s}l_{\rm s}$, where $l_{\rm s} = v_{\rm s}\tau_{\rm s}$ is the mean free path. In a dilute system, the velocity of the swimmer is essentially the isolated swimmer value, i.e. $v_{\rm s} \sim v_{\rm is}$. (Changes in swimming speed due to confinement do not affect the scaling predictions.) Deviations from this at larger concentrations will be discussed later. The mean free path scales as $l_{\rm s} \sim \ell^2(\sigma\psi_{\rm e})^{-1}$, where σ is a two-dimensional cross section (with units of length) for the redirections. Therefore, the swimmer diffusivity, $D_{\rm s}$, will scale as

$$D_{\rm s} \sim (\sigma\psi_{\rm e})^{-1}, \tag{18}$$

in dilute systems. Analysis for an unconfined domain [12] yields a similar scaling but with a three-dimensional cross section $\sigma_{\rm 3D}$ and the area fraction replaced by a volume fraction, so $D_{\rm s,3D} \sim (\sigma_{\rm 3D}\phi_{\rm e})^{-1}$.

We now turn to the fluid flow generated by the motion of the swimmers, considering the behavior of passive, non-Brownian tracers that follow the local fluid velocity. The tracers undergo ballistic motion at short lag times and diffusive motion at large lag times. The velocity of a tracer, $\mathbf{v}_{\rm t}$, is the fluid velocity at the location of the tracer $\mathbf{x}_{\rm t}$, and is the sum of the disturbance velocities due to each swimmer:

$$\mathbf{v}_{\rm t} = \mathbf{u}(\mathbf{x}_{\rm t}) = \sum_{\nu=i}^{N} \mathbf{u}_\nu^{\rm d}, \tag{19}$$

where $\mathbf{u}_\nu^{\rm d}$ is the disturbance at the position of the tracer due to swimmer ν. We can calculate the mean-squared velocity of the tracers by squaring this sum and performing an ensemble average over all possible configurations of the swimmers while the position of the tracer is held fixed at $\mathbf{x}_{\rm t}$:

$$\langle \mathbf{v}_{\rm t} \cdot \mathbf{v}_{\rm t} \rangle_{\mathbf{x}_{\rm t}} = \langle v_{\rm t}^2 \rangle_{\mathbf{x}_{\rm t}} = \sum_{\nu=1}^{N}\sum_{\mu=1}^{N} \langle \mathbf{u}_\nu^{\rm d} \cdot \mathbf{u}_\mu^{\rm d} \rangle_{\mathbf{x}_{\rm t}}, \tag{20}$$

where the subscript $\mathbf{x}_{\rm t}$ denotes that the tracer is held fixed at $\mathbf{x}_{\rm t}$ during the ensemble average over swimmers. The ensemble average without such a subscript means an average over all tracer positions has also been performed. In the dilute limit, we assume the swimmers to be distributed independently. This means that each swimmer is independently sampling a probability distribution for location within the channel, though that probability distribution need not be uniform. For example, we consider here that distribution to be peaked in a layer near each wall. The independence of the swimmers leads to

$$\langle v_{\rm t}^2 \rangle_{\mathbf{x}_{\rm t}} \sim N \left\langle \left(u_\nu^{\rm d}\right)^2 \right\rangle_{\mathbf{x}_{\rm t}} \sim \phi_{\rm e} \sim \psi_{\rm e}. \tag{21}$$

The number of swimmers N is proportional to both the volume fraction and the area fraction with a different proportionality factor that depends on the channel height.

A similar scaling analysis can be used for the tracer diffusivity, which can be written using the Green–Kubo relation [29, 30]

$$D_{\rm t} = \tfrac{1}{3}\int_0^\infty \langle \mathbf{v}_{\rm t}(0) \cdot \mathbf{v}_{\rm t}(t) \rangle \, {\rm d}t. \tag{22}$$

Again, we can replace the tracer velocity by a sum over swimmer disturbances. Assuming independent swimmers in the dilute limit gives

$$D_{\rm t} \sim \frac{N}{3}\int_0^\infty \left\langle \mathbf{u}_\nu^{\rm d}(0) \cdot \mathbf{u}_\nu^{\rm d}(t) \right\rangle {\rm d}t \sim \phi_{\rm e} \sim \psi_{\rm e}. \tag{23}$$

Combining the velocity and diffusivity scalings with the definition of a correlation time, $\tau_{\rm t} = D_{\rm t}/\langle v_{\rm t}^2 \rangle$ gives a prediction that $\tau_{\rm t}$ is independent of volume fraction in the dilute limit.

We can also use this behavior of the tracers to understand the correction to the swimmer behavior at finite concentration. The tracers represent a characteristic fluid element in the system. In addition to being self-propelled, each swimmer is advected by the local fluid disturbance (generated by the other

swimmers). If the fluid velocity does not change rapidly over the size of a swimmer, then we can write

$$\mathbf{v}_s \approx \mathbf{v}_{is} + \mathbf{v}_t(\mathbf{x}_s). \tag{24}$$

Squaring this expression and neglecting the cross terms in the dilute limit gives

$$\langle v_s^2 \rangle - v_{is}^2 \sim \langle v_t^2 \rangle. \tag{25}$$

Note that there exists a proportionality factor because the average over the fluid in the region occupied by the swimmers is different than the average over the fluid in the whole domain. The proportionality is replaced by an equality for an unconfined system, for which these domains are the same [12]. Combining this result with the scaling of the tracer velocity $\langle v_t^2 \rangle \sim \phi_e \sim \psi_e$ gives that:

$$\langle v_s^2 \rangle - v_{is}^2 \sim \phi_e \sim \psi_e. \tag{26}$$

and similarly that

$$\langle v_s^2 \rangle^{1/2} - v_{is} \sim \phi_e \sim \psi_e. \tag{27}$$

3.2. *Velocity fields and spatial correlations*

An important measure of correlations in a suspension of swimming micro-organisms is the spatial autocorrelation function of the fluid velocity. We will report results for correlations on planes of constant x_3. The separation of different fluid elements in this plane is denoted by $\mathbf{x}_\parallel$. Therefore, the fluid correlation is $C_f(\mathbf{x}_\parallel, x_3) = \langle \mathbf{u}(\mathbf{s}_\parallel, x_3) \cdot \mathbf{u}(\mathbf{s}_\parallel + \mathbf{x}_\parallel, x_3) \rangle$, where the angle bracket represents an ensemble average over swimmers and also an average over the tracer position $\mathbf{s}_\parallel$ in the plane $x_3 = \text{const}$.

A number of experimental studies [2, 3] have reported the spatial correlation function for the swimmer velocities: $C_s(\mathbf{x}_\parallel, x_3) = \langle \mathbf{v}_s(\mathbf{s}_\parallel, x_3) \cdot \mathbf{v}_s(\mathbf{s}_\parallel + \mathbf{x}_\parallel, x_3) \rangle$. Assuming the validity of the approximation given by equation (24), we can write that

$$\begin{aligned} C_s(\mathbf{x}_\parallel, x_3) = &\left\langle \mathbf{v}_{is}(\mathbf{s}_\parallel, x_3) \cdot \mathbf{v}_{is}(\mathbf{s}_\parallel + \mathbf{x}_\parallel, x_3) \right\rangle \\ &+ 2 \left\langle \mathbf{v}_{is}(\mathbf{s}_\parallel, x_3) \cdot \mathbf{u}(\mathbf{s}_\parallel + \mathbf{x}_\parallel, x_3) \right\rangle \\ &+ C_f(\mathbf{x}_\parallel, x_3). \end{aligned} \tag{28}$$

In the case of independent swimmers whose orientations are uncorrelated with the fluid velocity, this expression reduces to

$$C_s(\mathbf{x}_\parallel, x_3) = v_{is}^2 \chi_0(\mathbf{x}_\parallel) + C_f(\mathbf{x}_\parallel, x_3), \tag{29}$$

where $\chi_0(\mathbf{x}_\parallel) = 1$ if $\mathbf{x}_\parallel = 0$ and zero otherwise. This expression indicates the close relationship between C_s and C_f. In our simulations, C_f is substantially less susceptible to statistical noise than C_s so that is the quantity we report.

The correlation function C_s has been used in experiments and simulations to quantify the 'swirls' seen in the fluid [2, 3]. In particular, the existence of negative correlations has been used as evidence for collective behavior and used to quantify the size of the swirls. However, we will see here that negative correlations can be present even in the absence of collective behavior. The presence of the walls changes the disturbance that an organism produces in the fluid, and thus the correlations in the fluid.

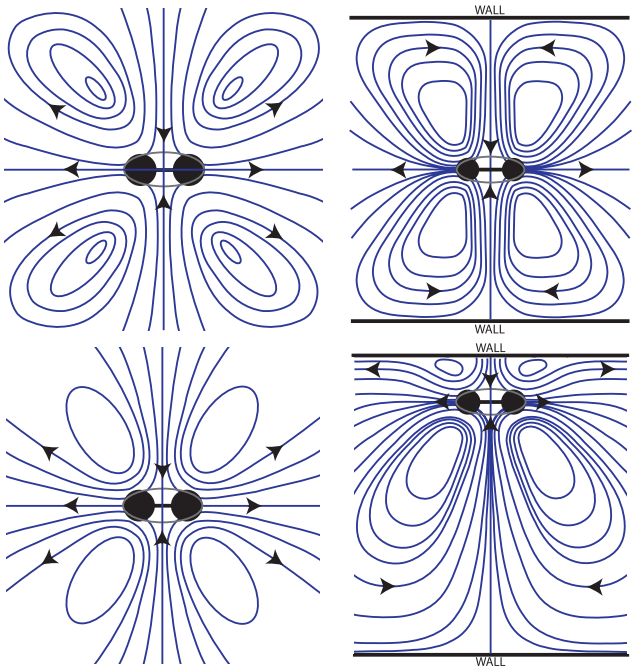

Figure 2. Streamlines of the fluid disturbance due to a force dipole representing a pusher: at the middle of the channel (top row) and close to the wall (bottom row). The fluid is shown in the x_1–x_2 plane (left column) and the x_1–x_3 plane (right column).

The spatial fluid correlations are determined by the fluid disturbance caused by a single swimmer as well as correlations between the swimmers. We consider here the correlations present in the absence of correlations between the swimmers, that is for independent swimmers. The correlation for independent swimmers is determined solely by the disturbance caused by a single swimmer and the concentration of swimmers. Recall from figure 1 the disturbance that a single swimmer produces in the fluid in the absence of walls, a pusher expels fluid out from the front and back, while sucking in fluid from the sides. However, the streamlines do not form closed loops, or swirls. Contrast this with figure 2, which shows the streamlines of the disturbance produced by a single swimmer in the presence of walls. The walls induce swirls in the flow. Two new length scales, the separation of the walls and the separation of a swimmer from the walls, affect the fluid structures.

The difference between these flow fields leads to different fluid correlations. As we show below, the swirl in the fluid induced by the wall means that even independent swimmers, that have no collective behavior, will produce fluid correlations that are negative. To illustrate this point, it is useful to visualize snapshots of a typical velocity field generated by these independent swimmers, as shown in figure 3. It is important to note that these snapshots are simply a sum of disturbances due to independent swimmers, each producing a disturbance like that in figure 2. The snapshots look remarkably similar to the results of simulations and experiments for which the swirls were considered evidence of collective behavior.

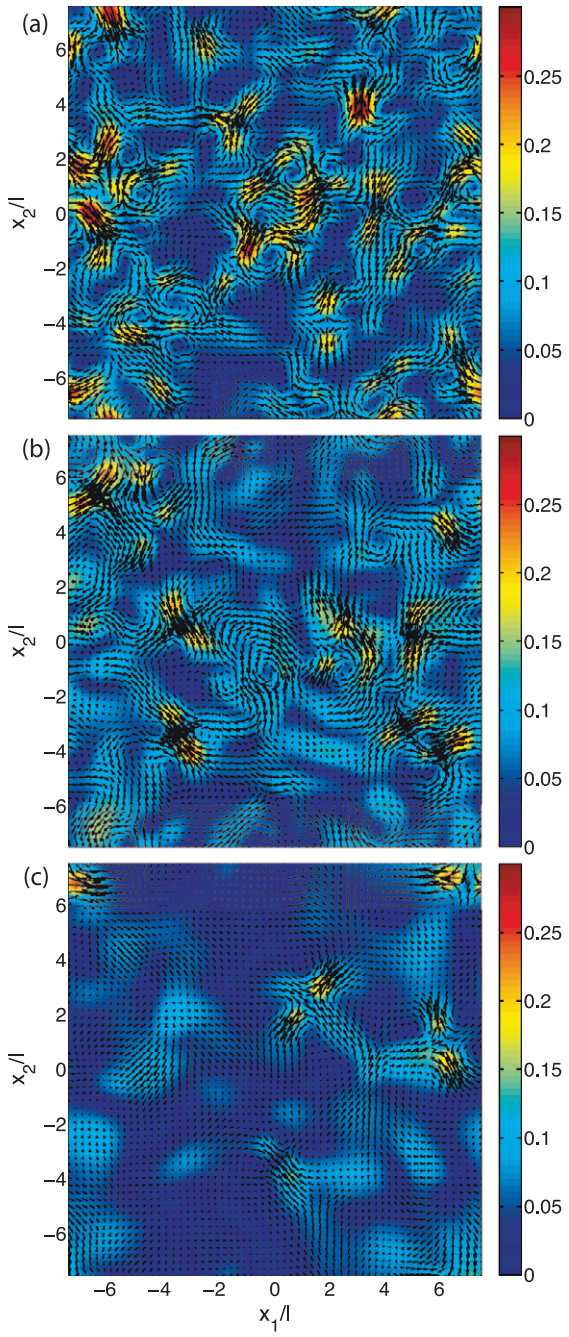

Figure 3. Snapshots of the velocity field for independent swimmers in layers at $\phi_e = 0.1$ ($\psi_e = 0.375$) with $L = 15\ell$ and $2H = 5\ell$. (a) $x_3 = 0.8H\ell$, (b) $x_3 = 0.5H\ell$ and (c) $x_3 = 0$.

The autocorrelation function within a fluid for which there are such swirls has a region of negative correlation, which is shown in figure 4. The correlation function has been calculated in two planes, the plane in which the swimmers form layers as well as the center plane of the slit. By changing the amount of confinement, we see that the length scale at which the correlation becomes negative in the center of the slit is the separation of the walls. However, the correlation near the wall, in the plane of the swimmers, is independent of the confinement. Instead, the length scale depends on the size of a swimmer and the separation of the swimmers from the wall.

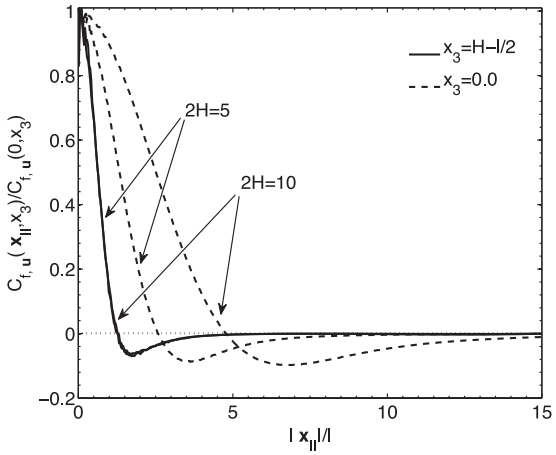

Figure 4. Fluid velocity autocorrelation function for independent swimmers at $2H = 5\ell$ and 10ℓ. The autocorrelation is normalized by the corresponding value at $|\mathbf{x}_\parallel| = 0$. When $x_3 = H - \ell/2$ the curves for $2H = 5\ell$ and 10ℓ are indistinguishable.

This is true for the cases shown because the second wall is far enough away that its effect on the fluid correlation is small.

By examining theoretically the fluid correlations generated by uncorrelated swimmers, we have shown that collective behavior is not necessary to generate swirls and negative correlations in the fluid. This illustrates the importance of comparing properties calculated from a suspension of swimming organisms to that of independent organisms to gauge the importance of collective behavior in producing the observed response.

4. Computational results

The theory just described makes distinct predictions regarding swimmer and tracer diffusivities, velocities, and fluid phase correlations. In this section we directly compute these quantities and others for suspensions over a range of concentrations and degrees of confinement. For the remainder of the article, all lengths are non-dimensionalized by the swimmer size ℓ and all times are non-dimensionalized by ℓ/v_{is}.

Let us start by fixing the confinement to five swimmer sizes, $2H = 5$, and the periodicity at three times the confinement, $L = 3 \times 2H$. We will show later that this periodicity is large enough for the results to be independent of L because the walls prevent formation of flow structures larger than the confinement. In the dilute theory described previously, it was assumed that the swimmers formed a layer at each wall. The formation of layers close to the confining wall in the simulations is illustrated in figure 5, which shows the swimmer concentration profiles as functions of x_3 at different effective volume fractions. Results for both pushers and pullers are shown, as well as for swimmers where hydrodynamic effects are completely neglected. For very dilute systems, the results in all cases are fairly similar—layers form near each wall and there is a nearly zero concentration at small distances from the walls due to steric exclusion of beads from the walls. However, the structure within the layer does depend on whether hydrodynamic interactions are included. With

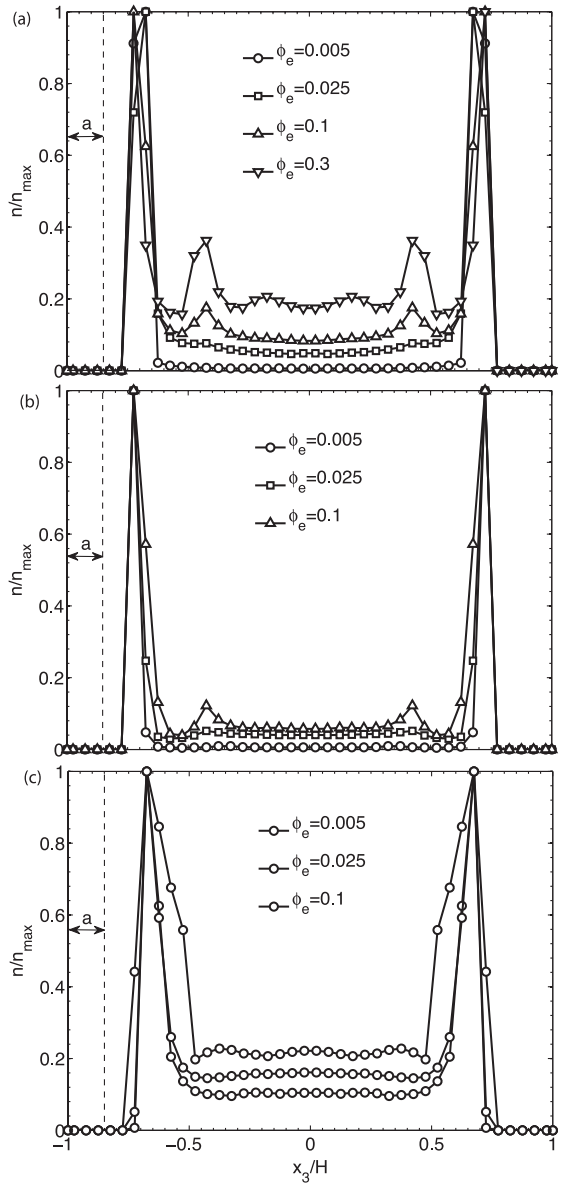

Figure 5. Concentration profile as a function of wall-normal position x_3 for different effective volume fractions with $L = 15$ and $2H = 5$. (a) Pushers, (b) pushers without hydrodynamic interactions and (c) pullers.

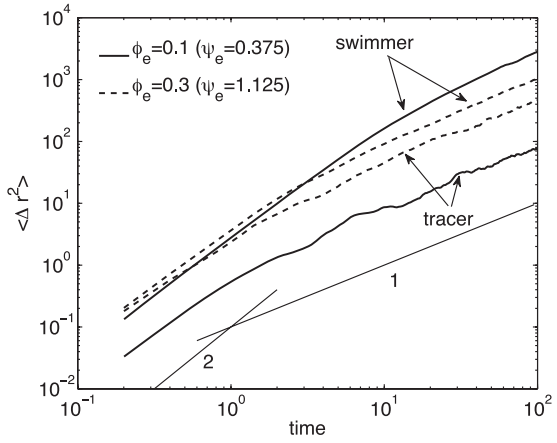

Figure 6. Mean-squared displacement versus time for swimmers and tracers at various concentrations with $L = 15$ and $2H = 5$.

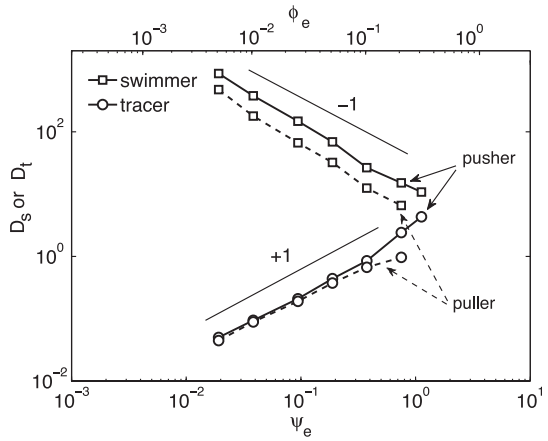

Figure 7. Diffusion coefficients as a function of the effective volume fraction (top axis) and effective area fraction (bottom axis) for swimmers and tracers with $L = 15$ and $2H = 5$.

hydrodynamic interactions, no long-range orientational order is observed in the layer. Without hydrodynamic interactions, a two-dimensional nematic state is observed, similar to the three-dimensional nematic state observed in an unconfined system without hydrodynamic interaction [12]. Once the concentration is high enough that the layer close to the wall is saturated, the swimmers form additional layers indicated by the secondary peaks in the profiles at high concentrations.

Figure 6 shows the mean-squared displacement (MSD) in the periodic (x_1, x_2) plane as a function of time, for swimmers and fluid tracers, at two concentrations: $\phi_e = 0.1$ ($\psi_e = 0.375$) and $\phi_e = 0.3$ ($\psi_e = 1.125$). At short times, the MSD is ballistic, reflecting the straight-line motions of an isolated swimmer. The duration of this ballistic regime decreases as the concentration increases. At longer times the behavior becomes diffusive. Since Brownian motion is absent, the origin of this diffusive regime is the interactions between the swimmers. Figure 7 shows the long-time diffusion coefficients D_s and D_t as a function of the effective volume fraction and area fraction. At low concentrations the swimmers have a high effective diffusion coefficient reflecting the weak hydrodynamic interactions between them. The flow is only disturbed by a small number of swimmers so tracers diffuse very slowly. As the concentration is increased the diffusivity of the swimmers decreases, as the natural ballistic trajectories are increasingly perturbed by hydrodynamic interactions and collisions with other swimmers. Correspondingly, the naturally motionless tracers feel the motion of increasingly more swimmers and their diffusivity increases.

According to the results in figure 7, the diffusion coefficient for both swimmers and tracers follow the dilute theory scalings ($D_s \sim \psi_e^{-1}$, $D_t \sim \psi_e$) developed in section 3 even at moderate concentrations. Note the difference in diffusivity and density profiles compared to our previous work [8]. For the volume fractions shown in the present work, we do not see the same dramatic increase in diffusivity and

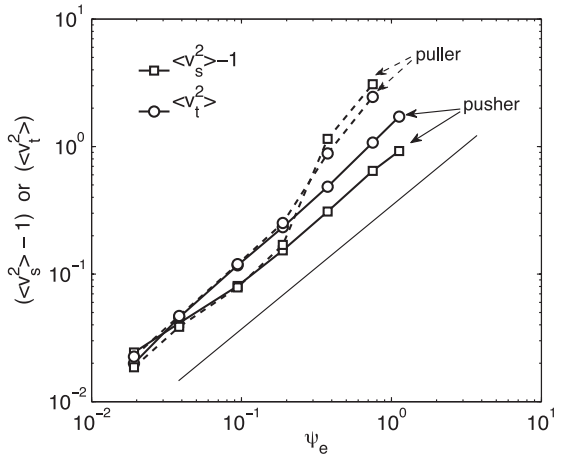

Figure 8. Mean-squared velocity for swimmers, $\langle v_s^2\rangle - 1$, and tracers, $\langle v_t^2\rangle$ as a function of the effective area fraction for $L = 15$ and $2H = 5$.

shift in the density profiles to the center of the channel. These differences seem to be due to the use of regularized forces in the present work, versus point-forces in the former, and an excluded volume potential as shown in figure 1. With this excluded volume potential and swimmer aspect ratio, obtaining much larger volume fractions is not possible because there is a largest volume fraction corresponding to the close-packed state.

From section 3, we saw that the diffusivities in figure 7 are related to the typical velocities of the swimmers and tracers. Figure 8 shows $\langle v_t^2\rangle$ and $\langle v_s^2\rangle - 1$ as functions of ψ_e. Both display an approximately linear increase with concentration, as predicted by the simple theory. We believe the deviation at small concentration is because of statistical errors due to the small number of swimmers in the domain at small concentrations. As with the diffusivities, the dilute scaling seems to hold even at concentrations well above $\psi_e = 0.1$ for pushers. However, the puller simulations deviate from the dilute scaling at $\psi_e \gtrsim 0.2$. The cause for this difference between pushers and pullers is unknown.

The final property we examine for this initial confinement is the fluid flow generated by the swimmers. Figure 9 shows snapshots of the fluid velocity field after more than 1000 dimensionless times in a plane near the wall of the channel ($x_3 = 0.8H$) for different concentrations $\phi_e = 0.01, 0.1$ and 0.3 ($\psi_e = 0.0384, 0.375$ and 1.125). These velocity fields are similar to those observed in some experiments [2]. Snapshots suggest that the size of the flow structures is related to the wall separation $2H$ (as we will address later). We also examined the snapshots for three different locations in the channel, $x_3 = 0, 0.5H$, and $0.8H$, which are shown in figure 10 for $\phi_e = 0.1$ ($\psi_e = 0.375$).

We now turn to the effect of the degree of confinement on the results. Simulations with a wider gap ($2H = 10$ and $L = 3\times 2H$) will be examined as well as a highly confined case of $2H = 1$, $L = 20 \times 2H$, and with the swimmers restricted to lie in the midplane of the channel—a monolayer. Figures 11 and 12 show the long-time diffusion coefficients D_t and D_s,

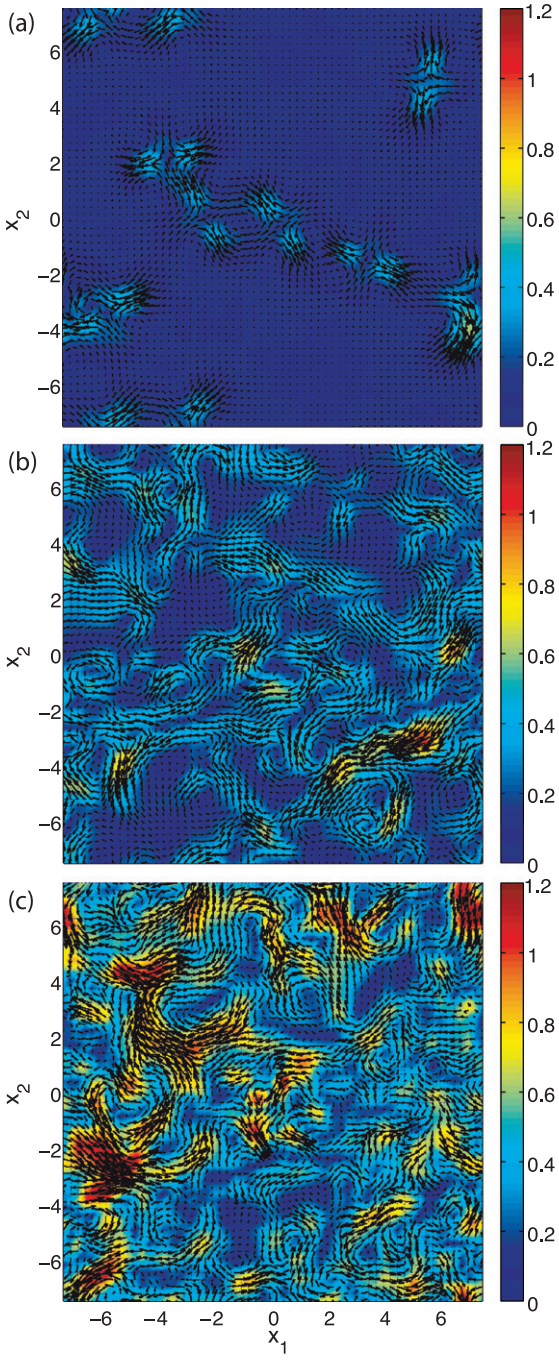

Figure 9. Snapshots of the velocity field at $x_3 = 0.8H$ ($x_3 = H - 1/2$) with $L = 15$ and $2H = 5$. (a) $\phi_e = 0.01$ ($\psi_e = 0.0383$) (b) $\phi_e = 0.1$ ($\psi_e = 0.375$) (c) $\phi_e = 0.3$ ($\psi_e = 1.125$).

the mean-squared swimmer velocity deviation $\langle v_s^2\rangle - 1$, and the mean-squared fluid velocity $\langle v_t^2\rangle$ for all three confinements. The first observation is that all confinements follow the dilute theory scalings at low concentrations. In particular, we see that the swimmer diffusivities for $2H = 5$ and 10 confinements collapse reasonably well when the concentration is represented as an effective area fraction. This supports the simple theory that assumes the swimmers form a layer next to each wall in the dilute limit. The swimmer diffusivities in the monolayer have

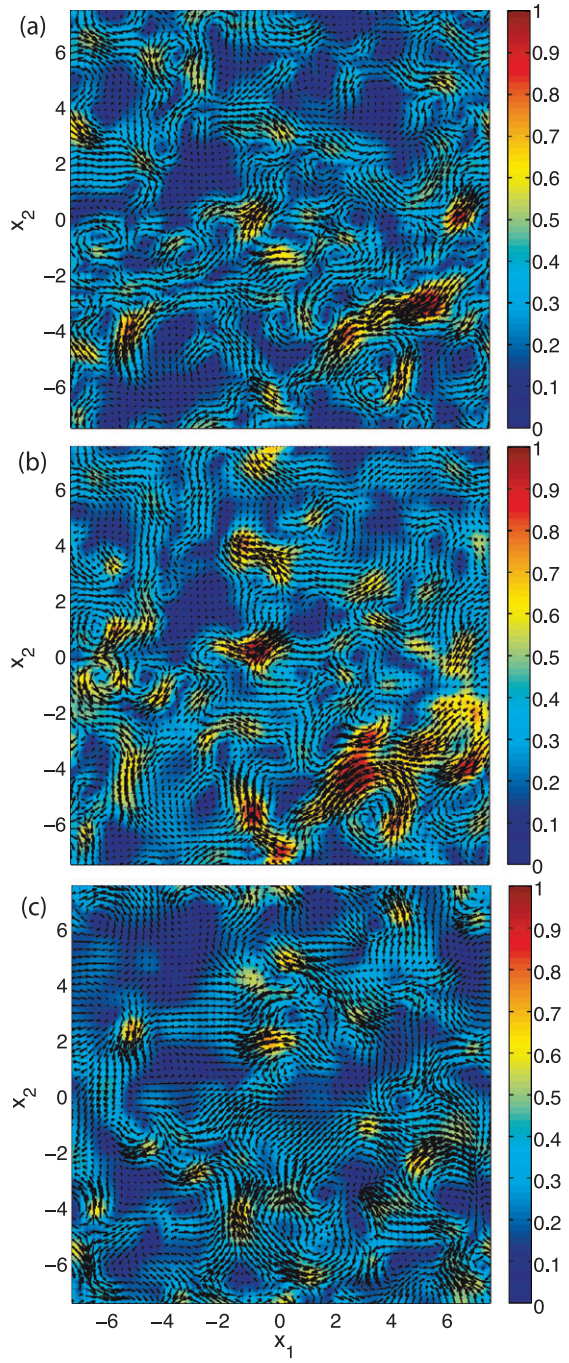

Figure 10. Snapshots of the velocity field for $\phi_e = 0.1$ ($\psi_e = 0.375$) with $L = 15$ and $2H = 5$. (a) $x_3 = 0.8H$ ($x_3 = H - 1/2$), (b) $x_3 = 0.5H$ and (c) $x_3 = 0$.

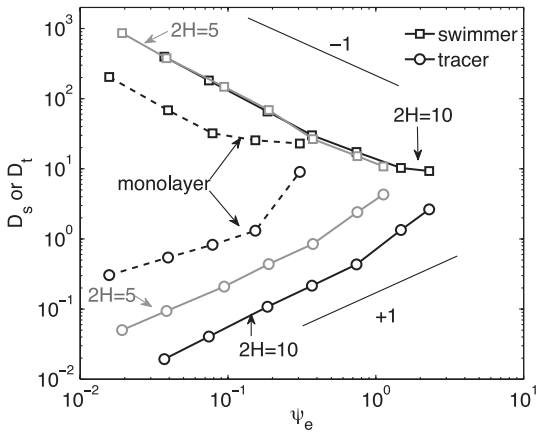

Figure 11. Diffusion coefficients versus effective area fraction for swimmers and tracers for different confinements. For $2H = 5$ and 10 we used $L = 3 \times 2H$, while for the monolayer $2H = 1$ we used $L = 20 \times 2H$.

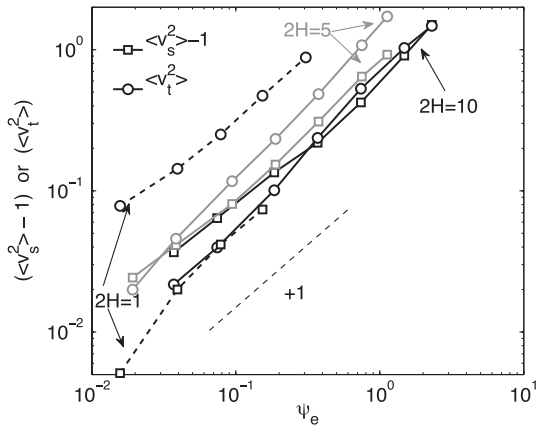

Figure 12. Mean-squared velocity for swimmers, $\langle v_s^2 \rangle - 1$, and tracers, $\langle v_t^2 \rangle$ versus effective area fraction. For $2H = 5$ and 10 we used $L = 3 \times 2H$, while for the monolayer $2H = 1$ we used $L = 20 \times 2H$.

the same scaling, though a different prefactor. This difference is most likely due to either a difference in the hydrodynamic interactions between swimmers in the monolayer because of the nearby walls or the inability of the swimmers to escape from the layer.

The tracer diffusivities, while following the simple scaling with area fraction, do not collapse with ψ_e with changing confinement. Because the tracers are not restricted to planes near the walls, at weak confinement (large H) the tracers can sample the lower velocities in the center of the channel, away from the swimmer layers near the walls. This difference results in a lower velocity of tracers with weaker confinement, as seen in figure 12.

From the earlier theoretical analysis, we found that uncorrelated swimmers produce swirls in the fluid, resulting in negative fluid correlations. The size of these negative regions were related to the separation of the walls, the size of a swimmer, and the separation of a swimmer from a wall. We found in the simulations swirls in the fluid as shown in figures 9 and 10. To make a quantitative comparison between the simulations and the theory of uncorrelated swimmers, we compare the fluid autocorrelation functions in planes parallel to the slit. Figure 13 shows the velocity autocorrelation function at two x_3-planes, $x_3 = 0.0$ and $0.8H$, for $2H = 5$ and 10, both with $L = 3 \times 2H$ and $\phi_e = 0.05$. These results indicate, as foreshadowed by the velocity fields, that the scale of the velocity autocorrelation is set by the distance between the walls. The fluid velocities are correlated at short length scales and, before they become decorrelated,

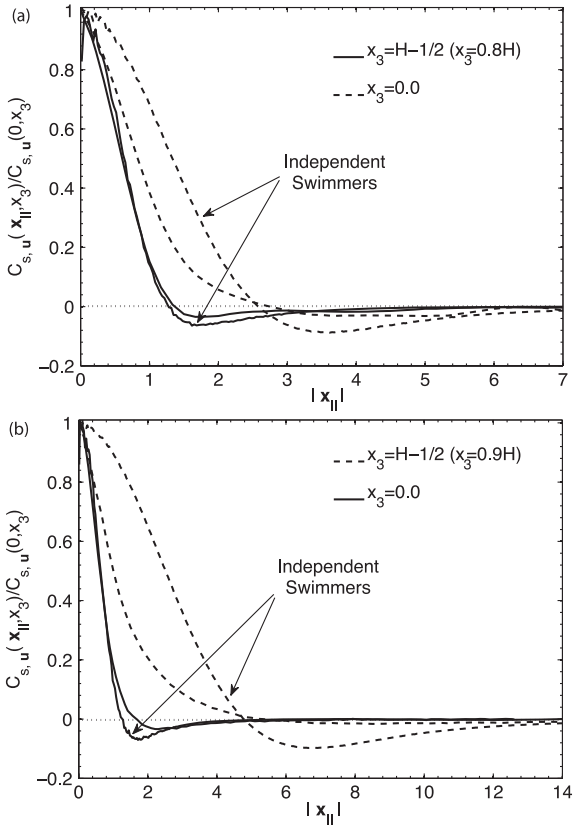

Figure 13. Fluid velocity autocorrelation function at $\phi_e = 0.05$. (a) $2H = 5$ ($\psi_e = 0.19$) and (b) $2H = 10$ ($\psi_e = 0.37$).

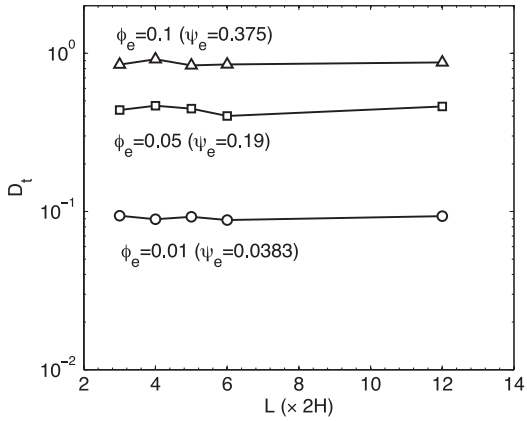

Figure 14. System size dependence of the tracer (fluid) diffusion coefficient at three effective volume fractions.

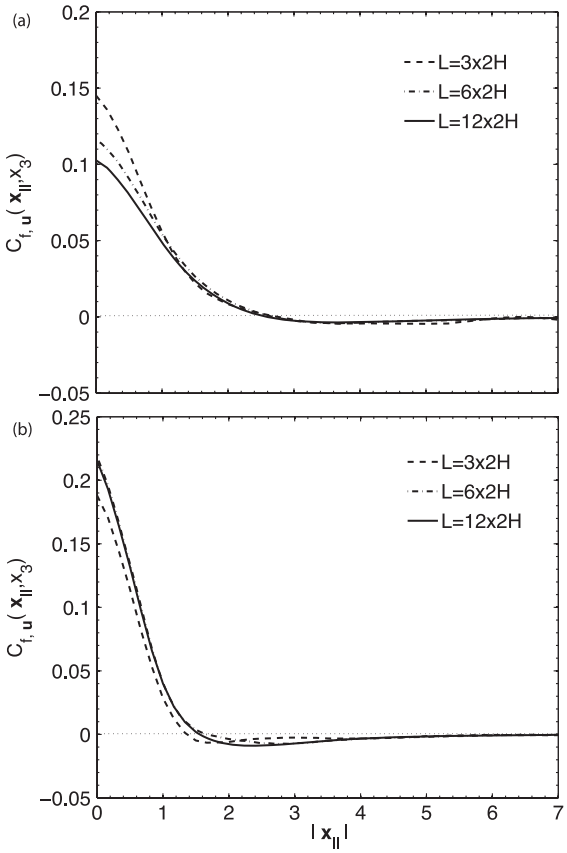

Figure 15. Fluid velocity autocorrelation function for $2H = 5$ at $\phi_e = 0.05$ ($\psi_e = 0.19$) as a function of the system size. (a) $x_3 = 0$ and (b) $x_3 = 0.8H$ ($x_3 = H - 1/2$).

there is an anticorrelation. While these types of negative correlations might be attributed to swirls caused by collective behavior, it is necessary to show an explicit comparison with the uncorrelated swimmer response because independent swimmers can produce negative correlations due to the change in hydrodynamics caused by the wall. Figure 13 shows such a comparison. First consider the comparison between curves in the plane $x_3 = 0.8H$. We see that the full simulation correlations are similar to the independent swimmer calculation. The difference between the curves in slightly larger in the plane $x_3 = 0$. Recall that the independent swimmers are all placed at the walls, which produce fluid correlations in the center of the channel. The full simulations however also have some swimmers in the center of the channel. This additional contribution from the swimmers in the center may be sufficient to account for the difference.

We now return to the issue of system size effects and our choice of L in the periodic directions. In order to explore the system size effects on the results, the confinement of $2H = 5$ was kept constant while the periodicity of the box was increased from $L = 3 \times 2H$ to $4 \times 2H, 5 \times 2H, 6 \times 2H$ and $12 \times 2H$. Underhill *et al* [12] found that the tracer diffusivity in a three-dimensional periodic unconfined system has a dependence on system size. Because the tracer diffusivity in the unconfined system had a stronger system size dependence than the swimmer diffusivity and the velocities, we show in figure 14 the system size dependence of the tracer diffusion coefficient in the confined domain. No system size dependence is observed. We also did not observe any system size dependence of the swimmer diffusivity or swimmer and tracer velocities. This explicitly justifies our use of $L = 3 \times 2H$ in the data presented earlier.

Finally, figure 15 illustrates the velocity autocorrelation at $2H = 5$ for three system sizes $L = 3 \times 2H, 6 \times 2H$ and $12 \times 2H$. The curves have a slight change with system size at small separations, though they seem to converge quickly with increasing system size. Clearly, the lack of changes

with a system size in the confined system compared to the unconfined system is due to the introduction of an additional length scale once the system is confined. This is not surprising because the confinement restricts flow structures larger than the confinement and modifies the hydrodynamic interactions between swimmers. If the collective behavior seen in the unconfined simulations is due to the long-range nature of the hydrodynamic interactions, screening of these interactions by the walls may affect the collective structures formed. The effect of hydrodynamic screening on the dynamics of polymers has been studied in detail [20, 31, 32]. In the polymer literature, it is the rate of decay of the fluid disturbance with distance (as well as the rotational symmetry) that determines if screening is present or not. At large enough distance from a swimmer in the confined domain, the velocity disturbance decays as r^{-3}. It is not clear if this decay is responsible for the results seen here—that the fluid structures do not depend on system size provided the periodicity is larger than the scale of confinement.

5. Conclusions

Simulations and theoretical analysis were used to study the dynamics of confined suspensions of self-propelled particles. The swimmers interact with one another via an excluded volume potential and hydrodynamic interactions through the fluid. These hydrodynamic interactions are altered by the confining walls.

We developed a simple theory of the motion of swimmers and tracers which captures the scalings of the diffusivity and velocities from the simulations. The theory assumes that in the dilute limit the swimmers form layers near the walls and execute a two-dimensional random walk within the layer. The theory also shows that even independent swimmers, with no collective behavior, can produce spatial fluid correlations in a confined domain that do not appear in an unconfined domain. This is particularly important because swirls in the fluid and negative correlations have been cited in previous studies as evidence of collective behavior. Using this theory, we were able to better understand how the scale of these negative correlations in the simulations change with the degree of confinement. In particular, the negative correlations in the center of the slit are governed by the separation of the walls, while the negative correlations near the walls are governed by the size of a swimmer and the separation of the swimmer from the wall. This is important for understanding experimental observations of swimming suspensions because many experiments are performed in the presence of walls.

Acknowledgments

We gratefully acknowledge support from NSF grants CTS-0522386 and DMR-0425880 (Nanoscale Science and Engineering Center).

References

[1] Mendelson N H, Bourque A, Wilkening K, Anderson K R and Watkins J C 1999 Organized cell swimming motions in *Bacillis subtilis* colonies: patterns of short-lived whirls and jets *J. Bacteriol.* **181** 600–9

[2] Dombrowski C, Cisneros L, Chatkaew S, Goldstein R E and Kessler J O 2004 Self-concentration and large-scale coherence in bacterial dynamics *Phys. Rev. Lett.* **93** 098103

[3] Cisneros L H, Cortez R, Dombrowski C, Goldstein R E and Kessler J O 2007 Fluid dynamics of self-propelled microorganisms, from individuals to concentrated populations *Exp. Fluids* **43** 737–53

[4] Sokolov A, Aranson I S, Kessler J O and Goldstein R E 2007 Concentration dependence of the collective dynamics of swimming bacteria *Phys. Rev. Lett.* **98** 158102

[5] Wu X-L and Libchaber A 2000 Particle diffusion in a quasi-two-dimensional bacterial bath *Phys. Rev. Lett.* **84** 3017–20

[6] Vicsek T, Czirók A, Ben-Jacob E, Cohen I and Shochet O 1995 Novel type of phase transition in a system of self-driven particles *Phys. Rev. Lett.* **75** 1226–9

[7] Baskaran A and Marchetti M C 2008 Hydrodynamics of self-propelled hard rods *Phys. Rev.* E **77** 011920

[8] Hernández-Ortiz J P, Stoltz C G and Graham M D 2005 Transport and collective dynamics in suspensions of confined swimming particles *Phys. Rev. Lett.* **95** 204501

[9] Saintillan D and Shelley M J 2007 Orientational order and instabilities in suspensions of self-locomoting rods *Phys. Rev. Lett.* **99** 058102

[10] Ishikawa T and Pedley T J 2007 Diffusion of swimming model micro-organisms in a semi-dilute suspension *J. Fluid Mech.* **588** 437–62

[11] Mehandia V and Nott P 2008 The collective dynamics of self-propelled particles *J. Fluid Mech.* **595** 239–64

[12] Underhill P T, Hernández-Ortiz J P and Graham M D 2008 Diffusion and spatial correlations in suspensions of swimming particles *Phys. Rev. Lett.* **100** 248101

[13] Bray D 2001 *Cell Movements: from Molecules to Motility* 2nd edn (New York: Garland)

[14] Saintillan D and Shelley M J 2008 Instabilities and pattern formation in active particle suspensions: kinetic theory and continuum simulations *Phys. Rev. Lett.* **100** 178103

[15] Soni G V, Jaffar Ali B M, Hatwalne Y and Shivashankar G V 2003 Single particle tracking of correlated bacterial dynamics *Biophys. J.* **84** 2634–7

[16] Soni G V, Ananthakrishna G and Shivashankar G V 2004 Probing collective dynamics of active particles using modulation force spectroscopy *Appl. Phys. Lett.* **85** 2414–6

[17] Liao Q, Subramanian G, DeLisa M P, Koch D L and Wu M 2007 Pair velocity correlations among swimming *Escherichia coli* bacteria are determined by force-quadrupole hydrodynamic interactions *Phys. Fluids* **19** 061701

[18] Bird R B, Curtiss C, Armstrong R C and Hassager O 1987 *Dynamics of Polymer Liquids: Kinetic Theory* 2nd edn, vol 2 (New York: Wiley)

[19] Allen M P and Germano G 2006 Expressions for forces and torques in molecular simulations using rigid bodies *Mol. Phys.* **104** 3225

[20] Jendrejack R M, Schwartz D C, Graham M D and de Pablo J J 2003 Effect of confinement on DNA dynamics in microfluidic devices *J. Chem. Phys.* **119** 1165–73

[21] Kim S and Karrila S 1991 *Microhydrodynamics: Principles and Selected Applications* (Boston, MA: Butterworth-Heinemann)

[22] Hernández-Ortiz J P, Graham M D and de Pablo J J 2007 Fast computation of many-particle hydrodynamic and electrostatic interactions in a confined geometry *Phys. Rev. Lett.* **98** 140602

[23] Hockney R W and Eastwood J W 1988 *Computer Simulation using Particles* (London: Taylor and Francis)

[24] Power H and Wrobel L C 1995 *Boundary Integral Methods in Fluid Mechanics* (Southampton: Computational Mechanics Publications)

[25] Frigo M and Johnson S G 1997 The fastest Fourier transform in the west *Technical Report MIT-LCS-TR-728* Massachusetts Institute of Technology, September 1997
[26] Frigo M and Johnson S G 2005 The design and implementation of FFTW3 *Proc. IEEE* **93** 216–31 (special issue on 'Program Generation, Optimization, and Platform Adaptation')
[27] Press W H, Teukolsky S A, Vetterling W T and Flannery B P 1992 *Numerical Recipes in Fortran 77* 2nd edn (Cambridge: Cambridge University Press)
[28] Berke A P, Turner L, Berg H C and Lauga E 2008 Hydrodynamic attraction of swimming microorganisms by surfaces *Phys. Rev. Lett.* **101** 038102
[29] Reichl L 1998 *A Modern Course in Statistical Physics* 2nd edn (New York: Wiley–Interscience)
[30] McQuarrie D 1976 *Statistical Mechanics* (New York: Harper Collins)
[31] Chen Y-L, Graham M D, de Pablo J J, Randall G C, Gupta M and Doyle P S 2004 Conformation and dynamics of single DNA in parallel-plate slit microchannels *Phys. Rev.* E **70** 060901
[32] Balducci A, Mao P, Han J and Doyle P S 2006 Double-stranded DNA diffusion in slitlike nanochannels *Macromolecules* **39** 6273–81